PIFON-EPT: MR-Based Electrical Property Tomography Using Physics-Informed Fourier Networks

Xinling Yu,

Department of Electrical and Computer Engineering, University of California, Santa Barbara, CA 93106 USA

José E. C. Serrallés [Member, IEEE],

Research Laboratory of Electronics, Department of Electrical Engineering and Computer Science, Massachusetts Institute of Technology, Cambridge, MA 02139 USA.

Ilias I. Giannakopoulos,

Bernard and Irene Schwartz Center for Biomedical Imaging, Department of Radiology, New York University Grossman School of Medicine, NY 10016 USA.

Ziyue Liu,

Department of Statistics and Applied Probability, University of California, Santa Barbara, CA 93106 USA.

Luca Daniel [Fellow, IEEE],

Research Laboratory of Electronics, Department of Electrical Engineering and Computer Science, Massachusetts Institute of Technology, Cambridge, MA 02139 USA.

Riccardo Lattanzi [Senior Member, IEEE],

Center for Advanced Imaging Innovation and Research (CAI^{2}R), and with the Bernard and Irene Schwartz Center for Biomedical Imaging, Department of Radiology, New York University Grossman School of Medicine, NY 10016 USA.

Zheng Zhang [Member, IEEE]

Department of Electrical and Computer Engineering, University of California, Santa Barbara, CA 93106 USA

Abstract

We propose Physics-Informed Fourier Networks for Electrical Properties (EP) Tomography (PIFON-EPT), a novel deep learning-based method for EP reconstruction using noisy and/or incomplete magnetic resonance (MR) measurements. Our approach leverages the Helmholtz equation to constrain two networks, responsible for the denoising and completion of the transmit fields, and the estimation of the object's EP, respectively. We embed a random Fourier features mapping into our networks to enable efficient learning of high-frequency details encoded in the transmit fields. We demonstrated the efficacy of PIFON-EPT through several simulated experiments at 3 and 7 tesla(T) MR imaging, and showed that our method can reconstruct physically consistent EP and transmit fields. Specifically, when only 20% of the noisy measured

(Corresponding author: Xinling Yu), (xyu644@ucsb.edu).

fields were used as inputs, PIFON-EPT reconstructed the EP of a phantom with   5% error, and denoised and completed the measurements with   1% error. Additionally, we adapted PIFON-EPT to solve the generalized Helmholtz equation that accounts for gradients of EP between inhomogeneities. This yielded improved results at interfaces between different materials without explicit knowledge of boundary conditions. PIFON-EPT is the first method that can simultaneously reconstruct EP and transmit fields from incomplete noisy MR measurements, providing new opportunities for EPT research.

Keywords

Electrical Property Mapping; Fourier Features Mapping; Magnetic Resonance Imaging; Physics Informed Neural Networks

I. INTRODUCTION

Electrical properties (EP), namely relative permittivity and electric conductivity, determine the interactions between electromagnetic waves and biological tissue [1], [2]. EP have the potential to be employed as biomarkers for pathologies such as cerebral ischemia [3], [4] and cancer [5]–[8]. EP could also be used to improve the effectiveness of existing therapeutic modalities such as radiofrequency hyperthermia [9]–[11].

Several EP tomography (EPT) methods have been proposed that are based on MR measurements, such as the magnetic transmit (B_1^+) or receive (B_1^-) field maps [12]–[22]. These techniques can be classified based on the form of Maxwell's equations (differential or integral) they use to fit the MR measurements. Differential methods, such as the Helmholtz EPT (H-EPT) [14] or the Convection-Reaction EPT (CR-EPT) [16], require the calculations of spatial derivatives of noisy measured B_1^+ maps, which lead to errors and artifacts in the reconstructions [23]. On the other hand, integral equation-based methods [19], [20] are robust to noise, but require computationally expensive iterative optimizations that rely on an accurate model of the transmit coils [24], [25] and fine-tuned regularization parameters.

Recently, data-driven deep learning-based methods have been introduced for EP reconstruction [26]–[29] to mitigate the noise amplifications and high computational cost of standard methods. These methods treat MR measurements and EP distributions as 2D images or 3D volumes, and train regression convolution neural networks as surrogate EP reconstruction models from simulated training data. These supervised learning-based techniques perform well in simulation, but they are not reliable in vivo due to the necessarily limited number of different cases included in the training data. To improve the generalization to in-vivo data, hybrid techniques that embed deep learning into conventional EP mapping methods were proposed [30], [31]. These hybrid methods use neural networks to generate initial guesses of EP for iterative reconstruction schemes [30], or diffusion and convection coefficients for the convection-reaction equation [31]. While these approaches improve generalization, several electromagnetic simulations are still required to generate training data, which can be very expensive and time-consuming, thus there is only a limited amount of available datasets. A recent hybrid technique directly reconstructs conductivity from

input transceive phases [32]. In such a method, a neural network is trained to represent the input transceive phase map, where the gradients of the phase are computed by automatic differentiation [33] and then used to solve the phase-only convection-reaction EPT. The reconstructed conductivity is compared with ground-truth values at the boundary, as a regularization for the neural network that represents the phase. Since this method retains the physics of EPT, it does not require a comprehensive set of electromagnetic simulations. However, learning a single neural network that can simultaneously represent the ground-truth phase and provide accurate gradient approximations directly from noisy measured phase maps is challenging, which is shown by the fact that they yielded highly inaccurate EP reconstructions in most cases.

Following our preliminary study [34], here we propose the Physics-Informed Fourier Networks (PIFONs) Electrical Properties Tomography (PIFON-EPT) framework, which leverages recent developments on physics-informed deep learning [35]–[38], and Fourier features mapping [39] to learn both the EP distribution and the B_1^+ field globally from noisy and/or incomplete $\widetilde{B}_1^+$ measurements. The proposed framework can efficiently de-noise the $\widetilde{B}_1^+$ measurements. Once trained, PIFONs can accurately predict the EP and B_1^+ field at any location within the PDE domain, enhancing high-resolution imaging capabilities. In contrast to integral equation-based methods [19], [20], which necessitate repeated simulations of forward equations, PIFONs tackle the inverse problem directly. This approach has the computational cost equivalent to solving a single forward equation. Differently from other supervised learning-based EPT methods [26]–[29], our proposed PIFON-EPT technique can reconstruct EP directly, without being trained on known B_1^+ and EP distribution pairs. Compared with recent physics-aware hybrid EPT methods [31], [32] in which EP are still solved numerically from convection-reaction equation with boundary condition, our method represents EP as a neural network constrained by the Helmholtz equations and does not require any prior EP information.

The rest of the paper is organized as follows: In Section II, we provide a brief overview of standard EPT methods. In Section III, we describe the proposed novel PIFON-EPT framework. In Section IV, we demonstrate the effectiveness of our PIFON-EPT with four representative numerical experiments. Further discussion is provided in Section V, whereas Section VI summarizes the main points of this work.

II. TECHNICAL BACKGROUND

A. Fundamental Helmholtz Equations in MRI

The relation between the magnetic field (**B**) and the EP of a medium can be described by the Helmholtz equation:

$$\nabla^2 \mathbf{B} + k_0^2 \varepsilon_c \mathbf{B} + \nabla \varepsilon_c \times \frac{\nabla \times \mathbf{B}}{\varepsilon_c} = 0,$$

(1)

where k_0 is the wave number in vacuum and

$$\varepsilon_c = \varepsilon_r - \frac{i\sigma}{\omega\varepsilon_0},$$

(2)

is the relative complex permittivity. Here, ε_r is the relative permittivity and σ is the electric conductivity, i denotes the imaginary unit, ω denotes the angular frequency, and ε_0 denotes the vacuum permittivity. Since the full transmit $\mathbf{B}_1$ cannot be measured in an MRI scanner, but only its positively rotating component $B_1^+ = (B_x + iB_y)/2$, we can re-write equation (1) with the help of Gauss' law ($\nabla \cdot \mathbf{B} = 0$) as:

$$\nabla^2 B_1^+ + k_0^2 \varepsilon_c B_1^+ = \left(\frac{\partial B_1^+}{\partial x} - i\frac{\partial B_1^+}{\partial y} + \frac{1}{2}\frac{\partial B_z}{\partial z} \right)(g_x + ig_y)$$
$$+ \left(\frac{\partial B_1^+}{\partial z} - \frac{1}{2}\frac{\partial B_z}{\partial x} - i\frac{1}{2}\frac{\partial B_z}{\partial y} \right)g_z.$$

(3)

Here, $\mathbf{g}: = (g_x, g_y, g_z): = \nabla \ln\varepsilon_c$. If we assume a smooth distribution of the EP, their gradient $\mathbf{g}$ can be ignored, and equation (3) becomes the *homogeneous Helmholtz equation*:

$$\nabla^2 B_1^+ + k_0^2 \varepsilon_c B_1^+ = 0.$$

(4)

B. Standard Differential EPT Methods

One can solve equations (3) and (4) for the EP, starting from measured B_1^+ maps. There are several methods based on such approach (here is a non-exhaustive list [14]–[21]). Next, we provide a brief overview of two popular ones: the Helmholtz EPT [14] and the Convection-Reaction EPT [16]. Both techniques require the knowledge of absolute phase of B_1^+, which, for birdcage coils, can be estimated with the transceive assumption [14]. Open-source software implementations of these methods can be found in EPTlib [40].

1) Helmholtz EPT: Assuming a homogeneous distribution of the EP and access to measured complex $\widetilde{B}_1^+$ maps, one can directly invert the homogeneous Helmholtz equation (4) to estimate the EP:

$$\varepsilon_c = -\frac{\nabla^2 \widetilde{B}_1^+}{k_0^2 \widetilde{B}_1^+}.$$

(5)

The second-order spatial derivatives of the measured $\widetilde{B}_1^+$ can be computed via finite difference approaches. If the measured fields are noisy, smoothing filters such as the 2nd order Savitzky-Golay filter [41] can be applied to improve the numerical derivatives.

2) Convection-Reaction EPT: High-field MRI scanners (< 7 T) utilize birdcage-based body coils [42] for transmission. In these cases, the B_z component of the coil's magnetic field can be assumed negligible near the mid-plane of the scanner bore. As a result, the generalized Helmholtz equation (3) can be simplified as:

$$\nabla^2 \widetilde{B}_1^+ + k_0^2 \varepsilon_c \widetilde{B}_1^+ = \left(\frac{\partial \widetilde{B}_1^+}{\partial x} - i \frac{\partial \widetilde{B}_1^+}{\partial y} \right)(g_x + i g_y)$$
$$+ \frac{\partial \widetilde{B}_1^+}{\partial z} \cdot g_z .$$

(6)

If we let $\gamma = 1/\varepsilon_c$, equation (6) can be rewritten as the convection-reaction equation with a zero diffusion term with respect to γ [16]:

$$\nabla^2 \widetilde{B}_1^+ \cdot \gamma + k_0^2 \widetilde{B}_1^+ = -\left(\frac{\partial \widetilde{B}_1^+}{\partial x} - i \frac{\partial \widetilde{B}_1^+}{\partial y} \right)\left(\frac{\partial \gamma}{\partial x} + i \frac{\partial \gamma}{\partial y} \right)$$
$$- \frac{\partial \widetilde{B}_1^+}{\partial z} \cdot \frac{\partial \gamma}{\partial z} .$$

(7)

By imposing appropriate boundary conditions (for example, the value of γ at the boundary of the domain), the convection-reaction equation (7) can be solved with a mesh-based finite difference scheme for γ. As for Helmholts EPT, also in this case the gradients of the measured $\widetilde{B}_1^+$ can be estimated using the Savitzky-Golay filter [41]. Since at MRI frequencies below 3 T, the absolute phase of B_1^+ is almost independent from the permittivity [13], it is possible to perform conductivity-only reconstructions using only the absolute phase of $\widetilde{B}_1^+$ [22]. It is also possible to include an artificial diffusion term to the convection-reaction equation to stabilize and improve the reconstruction results [43].

III. METHODS

Our proposed PIFON-EPT is a deep learning-based framework for robust EP estimation using noisy and/or incomplete complex-valued MR measurements. Note that since in MRI we do not have direct access to the absolute phase of B_1^+, we can rely on symmetry assumptions to estimate the complex-valued field in actual experiments. Specifically, at 1.5 and 3 tesla (T), when RF birdcage coils are used for transmission and reception in quadrature, the B_1^+ and B_1^- phases are approximately equal [13], [14]. Therefore, since the transceive phase is measurable [44], we can approximate the absolute phase of B_1^+ as half the transceive phase. The goal of PIFON-EPT is to learn the EP distributions globally that best describe the complex-valued B_1^+ at any spatial location (x, y, z), given $\left\{ \left(\boldsymbol{r}_i, \widetilde{B}_1^+(\boldsymbol{r}_i) \right) \right\}_{i=1}^{N}$ only for a limited N locations $\boldsymbol{r}_i = (x_i, y_i, z_i)$. The workflow of PIFON-EPT is summarized in Fig. 1.

A. PIFON-EPT workflow

Traditional EPT methods based on finite difference approximation of derivatives of B_1^+ (5), (7) can lead to noise amplifications in the reconstructed EP distributions. To prevent this, we

seek to solve an optimization problem constrained by the measured data and physical laws using physics-informed deep learning [35]. We denote the Helmholtz equation that describes the physical laws that must be satisfied by B_1^+ in the general form on a d-dimension domain $\Omega \in \mathbb{R}^d$:

$$\mathcal{N}_r[B_1^+; \varepsilon(\boldsymbol{r})](\boldsymbol{r}) = 0,$$

(8)

where $\boldsymbol{r} \in \mathbb{R}^d$ is a spatial coordinate and $\mathcal{N}_r[\,\cdot\,; \varepsilon]$ is a symbolic representation of the Helmholtz equation (4) or (6). $\varepsilon(\boldsymbol{r})$ denotes the complex-valued EP at the location $\boldsymbol{r}$ and $B_1^+(\boldsymbol{r})$ describes the hidden B_1^+ field solution governed by equation (8). Given N noisy and/or incomplete measurements $\left\{ \boldsymbol{r}_i, \widetilde{B}_1^+(\boldsymbol{r}_i) \right\}_{i=1}^N$, we aim to learn the EP distributions ε as well as the B_1^+ for all $\boldsymbol{r}$. To do so, we define a Fourier neural network $\mathcal{B}_1^+(\boldsymbol{r}; \theta_1)$, constructed by Gaussian random Fourier features [39] followed by a fully-connected neural network with a set of weights and biases θ_1, to represent the complex B_1^+ field. The Gaussian random Fourier features mapping is defined as:

$$\gamma(\boldsymbol{r}) = \begin{bmatrix} \cos(\boldsymbol{Br}) \\ \sin(\boldsymbol{Br}) \end{bmatrix},$$

(9)

where each entry in $\boldsymbol{B} \in R^{m \times 3}$ is sampled from a Gaussian distribution $\mathcal{N}(0, s^2)$. $2m$ equals the width of the fully-connected neural network following the defined Fourier features and $s > 0$ is a task-specific hyperparameter. We use an additional fully-connected neural network $\varepsilon_c(\boldsymbol{r}; \theta_2)$ with independent weights and biases θ_2 to estimate the distribution of EP. Hereinafter, we refer to $\mathcal{B}_1^+(\boldsymbol{r}; \theta_1)$ and $\mathcal{E}_c(\boldsymbol{r}; \theta_2)$ as B_1^+ net and EP net, respectively. The PDE residual of (8) is transformed to:

$$\mathcal{R}(\boldsymbol{r}, \theta_1, \theta_2) := \mathcal{N}_r[\mathcal{B}_1^+(\boldsymbol{r}; \theta_1); \mathcal{E}_c(\boldsymbol{r}; \theta_2)](\boldsymbol{r}).$$

(10)

A good set of candidate parameters $\{\theta_1, \theta_2\}$ can be obtained by minimizing the following composite loss function via gradient descent [45]–[47] with the Adam optimizer [48]:

$$\begin{aligned}
\mathcal{L}(\theta_1, \theta_2) &= \mathcal{L}_{\text{data}}(\theta_1) + \lambda \mathcal{L}_r(\theta_1, \theta_2), \\
\mathcal{L}_{\text{data}}(\theta_1) &= \frac{1}{N} \sum_{N}^{i=1} \left| \text{Re}\{\mathcal{B}_1^+(\boldsymbol{r}_i; \theta_1)\} - \text{Re}\{\widetilde{B}_1^+(\boldsymbol{r}_i)\} \right|^2 \\
&\quad + \frac{1}{N} \sum_{N}^{i=1} \left| \text{Im}\{\mathcal{B}_1^+(\boldsymbol{r}_i; \theta_1)\} - \text{Im}\{\widetilde{B}_1^+(\boldsymbol{r}_i)\} \right|^2, \\
\mathcal{L}_r(\theta_1, \theta_2) &= \frac{1}{N} \sum_{i=1}^{N} |\mathcal{R}(\boldsymbol{r}_i, \theta_1, \theta_2)|^2.
\end{aligned}$$

(11)

$\mathscr{L}_{data}$ denotes the data mismatch and $\mathscr{L}_r$ denotes the PDE residual. λ denotes the weight coefficient in the loss function, which balances the two loss terms in the composite loss. We remark that λ is a hyperparameter that can either be specified by the user or be tuned automatically [49], [50]. All the derivatives of $\mathscr{B}_1^+(\boldsymbol{r}; \theta_1)$ and $\mathscr{E}_c(\boldsymbol{r}; \theta_2)$ with respect to the spatial coordinate $\boldsymbol{r}$ as well as the gradient of the loss function with respect to the neural network parameters $\{\theta_1, \theta_2\}$, are computed using automatic differentiation algorithms [33].

The workflow of our proposed PIFON-EPT (Fig. 1) can be summarized as follow. First, we define two separate fully-connected neural networks B_1^+ Net and EP Net ($\mathscr{E}_c(\boldsymbol{r}; \theta_2)$) to represent the B_1^+ and the EP, respectively. A random Fourier features mapping (see Fig. 1 green dotted box) is embedded B_1^+ Net to learn high frequency components of the target B_1^+ field solution more efficiently [39]. Second, B_1^+ Net and EP Net are trained jointly by minimizing a composite loss function that aims to fit the measured $\widetilde{B}_1^+$ data (see Fig. 1 blue dotted box), while satisfying the physics laws characterized by the PDE residual. The trained physics-informed B_1^+ Net and EP Net facilitate the generation of physically consistent B_1^+ and EP predictions at any desired spatial point, respectively (see Fig. 1 bottom red dotted boxes). In particular the B_1^+ Net denoises and completes the input $\widetilde{B}_1^+$.

B. Choice of Helmholtz equation

If we assume piece-wise constant EP, then the Helmholtz equation simplifies as in (4). Eq. (6) is a generalized form of the same equation, which accounts for gradients of EP, but is yet not fully general because to reduce the number of unknowns, we assumed that B_z is equal to zero. Depending on which Helmholtz equation is used, we introduced two variants of PIFON-EPT: *simplified PIFON-EPT* and *generalized PIFON-EPT*.

1) Simplified PIFON-EPT: Assumes piece-wise constant EP and does not require any assumption on B_z. Following Eq. (4), the Helmholtz residual (10) can be represented as:

$$\mathscr{R}_H = \nabla^2 \mathscr{B}_1^+(\boldsymbol{r}; \theta_1) + k_0^2 \mathscr{E}_c(\boldsymbol{r}; \theta_2) \mathscr{B}_1^+(\boldsymbol{r}; \theta_1).$$

(12)

2) Generalized PIFON-EPT: Assumes $B_z \approx 0$ and uses the generalized equation (6). The Helmholtz residual (10) becomes:

$$\mathscr{R}_{GH} = \nabla^2 \mathscr{B}_1^+(\boldsymbol{r}; \theta_1) + k_0^2 \mathscr{E}_c(\boldsymbol{r}; \theta_2) \mathscr{B}_1^+(\boldsymbol{r}; \theta_1) - \frac{1}{\mathscr{E}_c(\boldsymbol{r}; \theta_2)}$$
$$\left(\frac{\partial \mathscr{B}_1^+(\boldsymbol{r}; \theta_1)}{\partial x} - i \frac{\partial \mathscr{B}_1^+(\boldsymbol{r}; \theta_1)}{\partial y} \right) \left(\frac{\partial \mathscr{E}_c(\boldsymbol{r}; \theta_2)}{\partial x} + i \frac{\partial \mathscr{E}_c(\boldsymbol{r}; \theta_2)}{\partial y} \right)$$
$$- \frac{1}{\mathscr{E}_c(\boldsymbol{r}; \theta_2)} \left(\frac{\partial \mathscr{B}_1^+(\boldsymbol{r}; \theta_1)}{\partial z} \cdot \frac{\partial \mathscr{E}_c(\boldsymbol{r}; \theta_2)}{\partial z} \right).$$

(13)

Both techniques rely on knowledge of the absolute phase of B_1^+, which for a quadrature birdcage coil can be estimated from the transceive phase assumption. Note that with a sufficient number of transmit-receive coils, it is theoretically possible to solve for both the

unknown absolute phase and B_z [51], although the lack of suitable multi-channel coils and the computational complexity of such solution has prevented practical implementations.

IV. RESULTS

We present a series of numerical examples to demonstrate the effectiveness of our proposed PIFON-EPT framework. Throughout all experiments, unless otherwise specified, we used simulated complex B_1^+ maps as measured data and corrupted them with white Gaussian noise with a standard deviation equal to the ratio of the peak value of $|B_1^+|$ to a prescribed peak signal-to-noise-ratio (SNR) value. The simulations were performed with the volume [52] and the volume-surface integral equation [53], [54] methods. The volume equations were solved using higher-order polynomials [55] as basis functions to ensure accuracy in the B_1^+ distributions. All experiments were performed on a server running Ubuntu 20.04.3 LTS operating system, with an Intel(R) Xeon(R) Silver 4216 CPU at 2.10GHz, 64 cores, 2 threads per core, and an NVIDIA RTX 3090 GPU with 24 GB of memory.

To measure the discrepancy between the prediction ($\hat{v}$) and ground-truth ($v \in \mathbb{R}^N$) values we used the peak normalized absolute error (PNAE), defined as:

$$\text{PNAE}(\hat{v}, v) = \frac{\| v - \hat{v} \|_1}{\| v \|_\infty}.$$

(14)

A. Validation against the analytical solution

To verify our method, we used a complex B_1^+ map obtained from the Mie Scattering theory [56] for an infinitely long homogeneous dielectric cylinder of relative permittivity 3 and electric conductivity 0.01 S/m, and it's air outside the cylinder. The operating wavelength was $\lambda = 2.437$ m and the cylinder had a radius r equal to the wavelength. A TMz planewave was used as the excitation.

1) Data Acquisition: We considered a representative section of the cylinder and computed the B_1^+ field distribution in the domain $[-2r, 2r] \times [-2r, 2r]$ using Mie scattering theory [57]. The pixel isotropic resolution was set to 0.05λ so that the section was 81×81 for a total of 6561 voxels. We corrupted the synthetic B_1^+ field with Gaussian noise of peak SNR of 200 and then scaled the noisy field with the peak value of $|B_1^+|$ to obtain synthetic $\widetilde{B}_1^+$ measurements. The resulting $\widetilde{B}_1^+$ fields were used as the measured data for PIFON-EPT.

2) PIFON Training Settings: B_1^+ Net was constructed by a Fourier features mapping initialized with $s = 2$ as a coordinate embedding of the input, followed by a fully-connected neural network with 3 layers, 128 units per layer. EP Net was constructed using a fully-connected neural network with 3 layers, 128 units per layer. We set all the activation functions as the Sine function. We set $\lambda = 10^{-4}$ in equation (11). We trained B_1^+ Net and EP Net jointly using the Adam optimizer for 120k iterations in total, with a decaying schedule of learning rates 10^{-3}, 10^{-4}, 10^{-5} decreased every 40k iterations, which took

~ 30 minutes and ~ 40 minutes for employing simplified PIFON-EPT and generalized PIFON-EPT, respectively.

3) Results: We tested the performance of the simplified and generalized PIFON-EPT using the same training settings. Fig. 2 and Fig. 3 compare the reconstructed EP against the ground truth values for the simplified and generalized PIFON-EPT, respectively. Fig. 4 and Fig. 5 compare ground truth and reconstructed B_1^+ maps for the simplified and generalized PIFON-EPT, respectively. The average PNAE over the domain for the relative permittivity, conductivity, and B_1^+ was 3.96%, 9.67% and 0.22%, respectively for the simplified PIFON-EPT. The error decreased to 1.80%, 1.11% and 0.20%, when the generalized PIFON-EPT was used. The lower error in this case is because the generalized PIFON-EPT is able to approximate better EPs at the boundary.

B. Concentric Cylindrical Phantom

We considered a two-compartment concentric cylindrical phantom with relative permittivity $\varepsilon = \{70, 78\}$ and conductivity $\sigma = \{0.5, 1\}$ S/m (outer, inner). The cylinder loaded a high-pass birdcage coil with eight legs as shown in Fig. 6. The outer and inner radius of the cylinder were 6 cm and 3 cm, respectively, and its length was 14 cm. For this example, we compared the proposed PIFON-EPT with the Helmholtz-EPT (H-EPT) and the Convection-Reaction EPT (CR-EPT) (see II-B). In particular, we used the implementations in EPTlib [40], with the Savitzky-Golay filter with an ellipsoid-shaped kernel of size $2 \times 2 \times 2$ to approximate all the gradients. For CR-EPT, we set the diffusion coefficient to 0.02 and the conductivity boundary condition to 0.55 S/m.

1) Data Acquisition: We used the volume-surface integral equation method [54] to simulate the circularly polarized (CP) mode of the birdcage coil loaded with the cylindrical phantom at 3 T. The resolution was set to 2 mm^3. We used B_1^+ and B_1^- from the central region of the cylinder ($12 \times 12 \times 2$ cm^3, MR measurements out of cylindrical phantom were not used) and corrupted them with Gaussian noise of peak SNR of 200. We approximated the complex B_1^+ using the transceive phase assumption (TPA) and constructed the MR measurements $\left|\tilde{B}_1^+\right|$ and $\tilde{\varphi}^\pm$.

2) PIFON Training Settings: The B_z field of a birdcage is negligible around the mid-plane of the coil. For this reason, we used the generalized PIFON-EPT to perform the reconstruction. For B_1^+ Net, the Fourier feature mapping was initialized with $s = 40$ as a coordinate embedding of the input, followed by a fully-connected neural network with 6 layers, 128 units per layer. EP Net was an additional Fourier neural network constructed by a Fourier feature mapping initialized with $s = 2$, followed by a fully-connected neural network with 6 layers, 128 units per layer. We set all the activation functions as the Sine function and set $\lambda = 10^{-8}$ in equation (11). We trained B_1^+ Net and EP Net jointly using the Adam optimizer for 120k iterations in total, with a decaying schedule of learning rates 10^{-3}, 10^{-4}, 10^{-5} decreased every 40k iterations. Note that the network settings have to change for different experimental setups". In particular, the total number of iterations is determined

based on the network size, and deep neural networks usually require more iterations to converge than shallow networks. The overall training time was 220 minutes on our GPU.

3) Results: The reconstructed EP (Fig. 7) and B_1^+ (Fig. 8) are presented for the central axial cut of the cylinder. The average PNAE over the entire volume of the cylinder was 4.84%, 3.20% and 0.25% for the relative permittivity, conductivity and B_1^+, respectively.

Fig. 9 and Fig. 10 present the conductivity reconstruction results for H-EPT and CR-EPT, respectively, along with the PNAE distribution and the error histogram. The average PNAE over the volume of the phantom was 51.80% and 11.28% for H-EPT and CR-EPT, respectively.

C. Four-Compartment Phantom

In this example, we explore the performance of PIFON-EPT at 7 T. We considered a previously used [19] tissue-mimicking four-compartment phantom shaped as a $20 \times 20 \times 20$ cm^3 rectangular parallelepiped. The relative permittivity values of the four compartments were 51, 56, 65, and 76. The corresponding electric conductivity values were 0.56, 0.69, 0.84, and 1.02 S/m.

1) Data Acquisition: We used a single external excitation to illuminate the phantom, generated from a numerical electromagnetic basis [58], similar to previous work [19]. We used 6 mm isotropic voxel resolution. We corrupted the synthetic B_1^+ with different levels of Gaussian noise (Peak SNR = 200, 100, 50, 20) and then scaled each field map by the corresponding peak value of $|B_1^+|$ to obtain synthetic $\tilde{B}_1^+$ measurements. The case of peak SNR = 50 is shown in Fig. 11.

2) PIFON Training Settings: Since the B_1 field in the z direction cannot be assumed zero at 7 T, we used the simplified PIFON-EPT. The B_1^+ Net was constructed using a Fourier feature mapping initialized with $s = 40$ as a coordinate embedding of the input, followed by a fully-connected neural network with 3 layers, 128 units per layer. For EP Net, we used a second fully-connected neural network with 3 layers, 128 units per layer. We set all the activation functions as the Sine function. We set $\lambda = 10^{-8}$ in equation (11). We trained B_1^+ Net and EP Net jointly using the Adam optimizer for 30k iterations in total, with a decaying schedule of learning rates 10^{-3}, 10^{-4}, 10^{-5} decreased every 10k iterations, which took 21.4 minutes on our GPU.

3) Results: Figs. 12 and 13 presents the reconstructed EP and B_1^+ map (absolute value and phase) for the central slice of the four-compartment phantom, respectively. Our method removed the noise from the noisy synthetic measurements (Fig. 11) and the reconstructed B_1^+ (Fig. 13) was indistinguishable from the noise-free ground truth. The average PNAE over the volume of the phantom was 2.47%, 4.01%, 0.24% for the relative permittivity, conductivity and B_1^+, respectively.

The average PNAE for the reconstructed EP and B_1^+ for different levels of noise in the synthetic measurements are summarized in TABLE I. The reconstructions were robust for a wide range of noise levels.

D. Incomplete Four-Compartment Phantom

In this final numerical experiment, we used the same four-compartment phantom as before, but we assumed the synthetic $\widetilde{B}_1^+$ measurements were incomplete, which could happen in reality if the measured MR signal used to reconstruct the B_1^+ maps is too low or corrupted for certain voxels. We tested whether PIFON-EPT could reconstruct the EP and a complete, denoised B_1^+ for the entire volume.

1) Data Acquisition: We randomly set to zero from 20% to 90% of the voxels in the synthetic $\widetilde{B}_1^+$ measurements with peak SNR of 50. As a result, only 10% to 80% of the measurements were used as input for simplified PIFON-EPT. Fig. 14 shows one of the resulting $\widetilde{B}_1^+$ measurements for the central axial cut, where 50% of the $\widetilde{B}_1^+$ values were set to zero.

2) Results: We used the same training settings as for the previous experiment. The total training time when we used 10%, 20%, 50%, and 80% of the measurements was 10, 11, 15, and 18 minutes, respectively. For the case where only 50% of the synthetic $\widetilde{B}_1^+$ measurements were used, Figs. 15 and 16 show the ground truth EP and noise-free synthetic B_1^+ (first column), the reconstructed EP and the denoised and completed B_1^+ (second column), and the PNAE of the predicted EP and B_1^+ (third column) for the central slice of the phantom. The fourth column presents the error distribution over the entire volume of the phantom. We found that our method could accurately reconstruct the EP and B_1^+ for the whole domain, despite using partial measurements as the input. The average PNAE over the entire volume of the phantom was 2.49%, 4.09% and 0.32% for the relative permittivity, conductivity, and B_1^+, respectively.

TABLE II summarizes the average PNAE for the EP and B_1^+ when different percentages of the synthetic measurements were used. The error for the B_1^+ reconstruction increased when a smaller percentage of the data was used. However, PIFON-EPT yielded robust results for the EP maps until as little as 20% of the measurements were used as inputs.

V. Discussion

In this work, we reformulated EPT as a physics-constrained optimization problem with the goal to train two independent neural networks (B_1^+ Net and EP Net) to represent the B_1^+ and EP at any location of interest. To achieve that, we minimized a composite loss that aims to fit $\widetilde{B}_1^+$ measurements while penalizing the PDE residual (see Fig. 1) via gradient descent with Adam optimizer [48]. Penalizing the PDE residual not only helps EP Net predict the EP distributions that best describe the measured data but also prevents B_1^+ Net from fitting the noise. Compared with standard EPT methods [14], [16] that rely on numerical derivatives to approximate gradients of noisy $\widetilde{B}_1^+$ measurements, which is prone to noise amplifications

and artifacts, PIFON-EPT uses automatic differentiation [33] to calculate all the necessary gradients from de-noised B_1^+ maps provided by B_1^+ Net. This way of computing derivatives makes our method robust to noise. Unlike previous supervised deep learning-based EPT methods [26]–[30], our approach does not require a large amount of known data pairs to supervise the training. Compared with previous hybrid deep learning EPT methods [31], [32], which combine deep learning and CR-EPT to solve EP from convection-reaction equations, our method directly trains a neural network (EP Net) to represent the EP based on measured data and the Helmholtz PDE without requiring any boundary conditions and hyperparameter tuning for the diffusion coefficient.

A major concern for B_1^+ maps represented by neural networks is that deep fully-connected networks could fail to learn high-frequency components of the target functions because of the spectral bias [59]–[62]. To overcome the spectral bias and ensure that B_1^+ Net would efficiently learn the high-frequency details of B_1^+, we applied Fourier features mapping as an input embedding to the B_1^+. In the concentric cylindrical phantom example, we also applied Fourier features mapping to EP Net because it could help the network avoid predicting homogeneous EP distributions.

In simplified PIFON-EPT, we assume a homogeneous distribution of EP. This assumption introduces errors near the interface between regions of different EP values and can deteriorate the quality of the reconstructions. When B_z is negligible, the generalized PIFON-EPT can be used which allows the estimation of inhomogeneous EP distributions based on the generalized Helmholtz equation (6) which can greatly decrease the errors near the tissue boundaries (see IV-A). In fact, we showed that PIFON-EPT returned 48.6% and 8.08% more accurate results on average compared to H-EPT and CR-EPT (see IV-B). Furthermore, CR-EPT required tuning of the boundary condition value and the diffusion coefficient parameter until the reconstructed conductivity was close to the ground-truth value, which is not practical in experiments where the ground-truth values are unknown.

To the best of our knowledge, PIFON-EPT is the only EPT method that can reconstruct EP and B_1^+ for an entire object, using incomplete and noisy B_1^+ measurements. We demonstrated this for an ultra-high field MRI example, using complex-valued synthetic B_1^+ measurements. The same approach would be impractical in actual experiments because the absolute phase of the B_1^+ is not measurable and the TPA does not hold at 7 T. However, note that PIFON-EPT could be adapted to work with multiple transmit coils, which could provide enough degrees of freedom to enable EP reconstruction using the relative phase of B_1^+ between the coil channels [19], [51], which can be measured. This approach will be explored in future work.

The current version of PIFON-EPT has a limitation when B_z can not be assumed equal to zero. In this case, boundary artifacts appearing in the reconstructed EP cannot be eliminated. Previous work suggests that this limitation could be overcome by using multiple transmit-receive coils [51]. In this work, we used instead a birdcage coil, for which B_z can be assumed negligible if the main field strength is lower or equal to 3T. However, we found that our network's expressive power was not enough to reconstruct both the EP and the B_1^+ in such

a case. To address this, we made our network deeper and used more complex architectures (for example, we included Fourier mapping also in the EP Net) to accurately represent the EP and B_1^+, which ultimately increased the network's training time. This problem could be solved by designing compressed network architectures [63], [64] to replace the current fully-connected neural networks.

VI. CONCLUSION

We introduced PIFON-EPT, a new technique to estimate EP and magnetic transmit field distributions from noisy and/or incomplete MR measurements. We demonstrated our new approach using a series of numerical examples, showing that PIFON-EPT is accurate and robust even when its input is corrupted with a significant amount of noise. Since PIFON-EPT can efficiently de-noise MR measurements, it has the potential to improve other MR-based EPT methods that rely on magnetic transmit fields as inputs. In future work, we will investigate the performance of the proposed algorithms with realistic human head models and perform experimental validation.

Acknowledgments

REFERENCES

[1]. Collins CM and Wang Z, "Calculation of radiofrequency electromagnetic fields and their effects in mri of human subjects," Magnetic resonance in medicine, vol. 65, no. 5, pp. 1470–1482, 2011. [PubMed: 21381106]

[2]. Hand J, "Modelling the interaction of electromagnetic fields (10 mhz–10 ghz) with the human body: methods and applications," Physics in Medicine & Biology, vol. 53, no. 16, p. R243, 2008. [PubMed: 18653928]

[3]. Holder D, "Detection of cerebral ischaemia in the anaesthetised rat by impedance measurement with scalp electrodes: implications for non-invasive imaging of stroke by electrical impedance tomography," Clinical Physics and Physiological Measurement, vol. 13, no. 1, p. 63, 1992. [PubMed: 1563222]

[4]. Fallert MA et al. , "Myocardial electrical impedance mapping of ischemic sheep hearts and healing aneurysms." Circulation, vol. 87, no. 1, pp. 199–207, 1993. [PubMed: 8419008]

[5]. Tha KK et al. , "Noninvasive evaluation of electrical conductivity of the normal brain and brain tumors," in Proc. Int. Soc. Magn. Reson. Med, vol. 22, 2014, p. 1885.

[6]. Tha KK et al. , "Noninvasive electrical conductivity measurement by mri: a test of its validity and the electrical conductivity characteristics of glioma," European radiology, vol. 28, no. 1, pp. 348–355, 2018.

[7]. Balidemaj E. et al. , "Feasibility of electric property tomography of pelvic tumors at 3t," Magnetic resonance in medicine, vol. 73, no. 4, pp. 1505–1513, 2015. [PubMed: 24777618]

[8]. Shin J. et al. , "Initial study on in vivo conductivity mapping of breast cancer using mri," Journal of Magnetic Resonance Imaging, vol. 42, no. 2, pp. 371–378, 2015. [PubMed: 25413153]

[9]. Rossmann C. and Haemmerich D, "Review of temperature dependence of thermal properties, dielectric properties, and perfusion of biological tissues at hyperthermic and ablation temperatures," Critical Reviews™ in Biomedical Engineering, vol. 42, no. 6, 2014.

[10]. Balidemaj E. et al. , "Hyperthermia treatment planning for cervical cancer patients based on electrical conductivity tissue properties acquired in vivo with ept at 3 t mri," International Journal of Hyperthermia, vol. 32, no. 5, pp. 558–568, 2016. [PubMed: 26982889]

[11]. de Oliveira MM, Wen P, and Ahfock T, "Bio-heat transfer model of electroconvulsive therapy: Effect of biological properties on induced temperature variation," in 2016 38th Annual International Conference of the IEEE Engineering in Medicine and Biology Society (EMBC). IEEE, 2016, pp. 3997–4000.

[12]. Haacke E. et al. , "Extraction of conductivity and permittivity using magnetic resonance imaging," Physics in Medicine & Biology, vol. 36, no. 6, p. 723, 1991.

[13]. Wen H, "Noninvasive quantitative mapping of conductivity and dielectric distributions using rf wave propagation effects in high-field mri," in Medical Imaging 2003: Physics of Medical Imaging, vol. 5030. SPIE, 2003, pp. 471–477.

[14]. Katscher U. et al. , "Determination of electric conductivity and local sar via b1 mapping," IEEE transactions on medical imaging, vol. 28, no. 9, pp. 1365–1374, 2009. [PubMed: 19369153]

[15]. Voigt T, Katscher U, and Doessel O, "Quantitative conductivity and permittivity imaging of the human brain using electric properties tomography," Magnetic Resonance in Medicine, vol. 66, no. 2, pp. 456–466, 2011. [PubMed: 21773985]

[16]. Hafalir FS et al. , "Convection-reaction equation based magnetic resonance electrical properties tomography (cr-mrept)," IEEE transactions on medical imaging, vol. 33, no. 3, pp. 777–793, 2014. [PubMed: 24595349]

[17]. Zhang X, Zhu S, and He B, "Imaging electric properties of biological tissues by rf field mapping in mri," IEEE transactions on medical imaging, vol. 29, no. 2, pp. 474–481, 2010. [PubMed: 20129847]

[18]. Sodickson DK et al., "Local maxwell tomography using transmit-receive coil arrays for contact-free mapping of tissue electrical properties and determination of absolute rf phase," in Proceedings of the 20th Annual Meeting of ISMRM. ISMRM Concord California, USA, 2012, p. 388.

[19]. Serrallés JE et al. , "Noninvasive estimation of electrical properties from magnetic resonance measurements via global maxwell tomography and match regularization," IEEE Transactions on Biomedical Engineering, vol. 67, no. 1, pp. 3–15, 2019. [PubMed: 30908189]

[20]. Leijsen RL et al. , "3-d contrast source inversion-electrical properties tomography," IEEE transactions on medical imaging, vol. 37, no. 9, pp. 2080–2089, 2018. [PubMed: 29994520]

[21]. Liu J. et al. , "Gradient-based electrical properties tomography (g ept): A robust method for mapping electrical properties of biological tissues in vivo using magnetic resonance imaging," Magnetic resonance in medicine, vol. 74, no. 3, pp. 634–646, 2015. [PubMed: 25213371]

[22]. Gurler N. and Ider YZ, "Gradient-based electrical conductivity imaging using mr phase," Magnetic resonance in medicine, vol. 77, no. 1, pp. 137–150, 2017. [PubMed: 26762771]

[23]. Mandija S. et al. , "Error analysis of helmholtz-based mr-electrical properties tomography," Magnetic resonance in medicine, vol. 80, no. 1, pp. 90–100, 2018. [PubMed: 29144031]

[24]. Giannakopoulos II et al., "Global Maxwell Tomography using an 8-channel radiofrequency coil: simulation results for a tissue-mimicking phantom at 7T," in 2019 IEEE International Symposium on Antennas and Propagation and USNC-URSI Radio Science Meeting. IEEE, 2019, pp. 823–824.

[25]. Giannakopoulos II et al. , "Magnetic-resonance-based electrical property mapping using Global Maxwell Tomography with an 8-channel head coil at 7 Tesla: a simulation study," IEEE Transactions on Biomedical Engineering, vol. 68, no. 1, pp. 236–246, 2020. [PubMed: 32365014]

[26]. Mandija S. et al. , "Opening a new window on mr-based electrical properties tomography with deep learning," Scientific reports, vol. 9, no. 1, pp. 1–9, 2019. [PubMed: 30626917]

[27]. Hampe N. et al. , "Investigating the challenges and generalizability of deep learning brain conductivity mapping," Physics in Medicine & Biology, vol. 65, no. 13, p. 135001, 2020.

[28]. Gavazzi S. et al. , "Deep learning-based reconstruction of in vivo pelvis conductivity with a 3d patch-based convolutional neural network trained on simulated mr data," Magnetic resonance in medicine, vol. 84, no. 5, pp. 2772–2787, 2020. [PubMed: 32314825]

[29]. Giannakopoulos I. et al. , "On the usage of deep neural networks as a tensor-to-tensor translation between mr measurements and electrical properties," Proc. ISMRM, 2020.

[30]. Leijsen R. et al. , "Combining deep learning and 3d contrast source inversion in mr-based electrical properties tomography," NMR in Biomedicine, vol. 35, no. 4, p. e4211, 2022. [PubMed: 31840897]

[31]. Inda AJG et al. , "Physics-coupled neural network magnetic resonance electrical property tomography (mrept) for conductivity reconstruction," IEEE Transactions on Image Processing, 2022.

[32]. Inda AJG et al. , "Physics informed neural networks (pinn) for low snr magnetic resonance electrical properties tomography (mrept)," Diagnostics, vol. 12, no. 11, p. 2627, 2022. [PubMed: 36359471]

[33]. Baydin AG et al. , "Automatic differentiation in machine learning: a survey," Journal of Marchine Learning Research, vol. 18, pp. 1–43, 2018.

[34]. Yu X. et al. , "MR-Based Electrical Property Reconstruction Using Physics-Informed Neural Networks," arXiv preprint arXiv:2210.12584, 2022.

[35]. Raissi M, Perdikaris P, and Karniadakis GE, "Physics-informed neural networks: A deep learning framework for solving forward and inverse problems involving nonlinear partial differential equations," Journal of Computational physics, vol. 378, pp. 686–707, 2019.

[36]. Karniadakis GE et al. , "Physics-informed machine learning," Nature Reviews Physics, vol. 3, no. 6, pp. 422–440, 2021.

[37]. Qi S. et al. , "Two-dimensional electromagnetic solver based on deep learning technique," IEEE Journal on Multiscale and Multiphysics Computational Techniques, vol. 5, pp. 83–88, 2020.

[38]. Qi S. and Sarris CD, "Electromagnetic-thermal analysis with fdtd and physics-informed neural networks," IEEE Journal on Multiscale and Multiphysics Computational Techniques, vol. 8, pp. 49–59, 2023.

[39]. Tancik M. et al. , "Fourier features let networks learn high frequency functions in low dimensional domains," Advances in Neural Information Processing Systems, vol. 33, pp. 7537–7547, 2020.

[40]. Arduino A, "Eptlib: An open-source extensible collection of electric properties tomography techniques," Applied Sciences, vol. 11, no. 7, p. 3237, 2021.

[41]. Savitzky A. and Golay MJ, "Smoothing and differentiation of data by simplified least squares procedures." Analytical chemistry, vol. 36, no. 8, pp. 1627–1639, 1964.

[42]. Hayes CE et al. , "An efficient, highly homogeneous radiofrequency coil for whole-body nmr imaging at 1.5 t," Journal of Magnetic Resonance (1969), vol. 63, no. 3, pp. 622–628, 1985.

[43]. Li C, Yu W, and Huang SY, "An mr-based viscosity-type regularization method for electrical property tomography," Tomography, vol. 3, no. 1, pp. 50–59, 2017. [PubMed: 30042971]

[44]. Brown RW et al., Magnetic resonance imaging: physical principles and sequence design. John Wiley & Sons, 2014.

[45]. Ruder S, "An overview of gradient descent optimization algorithms," arXiv preprint arXiv:1609.04747, 2016.

[46]. Yang Y. et al. , "Vflh: A following-the-leader-history based algorithm for adaptive online convex optimization with stochastic constraints," Available at SSRN 4040704, 2022.

[47]. Yang Y, Koppel A, and Zhang Z, "A gradient-based approach for online robust deep neural network training with noisy labels," arXiv preprint arXiv:2306.05046, 2023.

[48]. Kingma DP and Ba J, "Adam: A method for stochastic optimization," arXiv preprint arXiv:1412.6980, 2014.

[49]. Wang S, Yu X, and Perdikaris P, "When and why pinns fail to train: A neural tangent kernel perspective," Journal of Computational Physics, vol. 449, p. 110768, 2022.

[50]. Wang S, Teng Y, and Perdikaris P, "Understanding and mitigating gradient flow pathologies in physics-informed neural networks," SIAM Journal on Scientific Computing, vol. 43, no. 5, pp. A3055–A3081, 2021.

[51]. Sodickson DK et al., "Generalized local Maxwell tomography for mapping of electrical property gradients and tensors," in Proceedings of the 21st Annual Meeting of ISMRM. ISMRM, 2013, p. 4175.

[52]. Giannakopoulos II, Litsarev MS, and Polimeridis AG, "Memory footprint reduction for the FFT-based volume integral equation method via tensor decompositions," IEEE Transactions on Antennas and Propagation, vol. 67, no. 12, pp. 7476–7486, 2019.

[53]. Giannakopoulos II et al., "A tensor train compression scheme for remote volume-surface integral equation interactions," in 2021 International Applied Computational Electromagnetics Society Symposium (ACES). IEEE, 2021, pp. 1–4.

[54]. Giannakopoulos II et al. , "A hybrid volume-surface integral equation method for rapid electromagnetic simulations in mri," IEEE Transactions on Biomedical Engineering, 2022.

[55]. Georgakis IP et al. , "A fast volume integral equation solver with linear basis functions for the accurate computation of EM fields in MRI," IEEE Transactions on Antennas and Propagation, vol. 69, no. 7, pp. 4020–4032, 2020.

[56]. Wiscombe WJ, "Improved Mie scattering algorithms," Applied optics, vol. 19, no. 9, pp. 1505–1509, 1980. [PubMed: 20221065]

[57]. Bohren CF and Huffman DR, Absorption and scattering of light by small particles. John Wiley & Sons, 2008.

[58]. Georgakis IP et al. , "Novel Numerical Basis Sets for Electromagnetic Field Expansion in Arbitrary Inhomogeneous Objects," IEEE Transactions on Antennas and Propagation, vol. 70, no. 9, pp. 8227–8241, 2022. [PubMed: 37124164]

[59]. Ronen B. et al. , "The convergence rate of neural networks for learned functions of different frequencies," Advances in Neural Information Processing Systems, vol. 32, 2019.

[60]. Cao Y. et al. , "Towards understanding the spectral bias of deep learning," arXiv preprint arXiv:1912.01198, 2019.

[61]. Rahaman N. et al., "On the spectral bias of neural networks," in International Conference on Machine Learning. PMLR, 2019, pp. 5301–5310.

[62]. Wang S, Wang H, and Perdikaris P, "On the eigenvector bias of fourier feature networks: From regression to solving multi-scale pdes with physics-informed neural networks," Computer Methods in Applied Mechanics and Engineering, vol. 384, p. 113938, 2021.

[63]. Novikov A. et al. , "Tensorizing neural networks," Advances in neural information processing systems, vol. 28, 2015.

[64]. Liu Z, Yu X, and Zhang Z, "TT-PINN: A tensor-compressed neural PDE solver for edge computing," arXiv preprint arXiv:2207.01751, 2022.
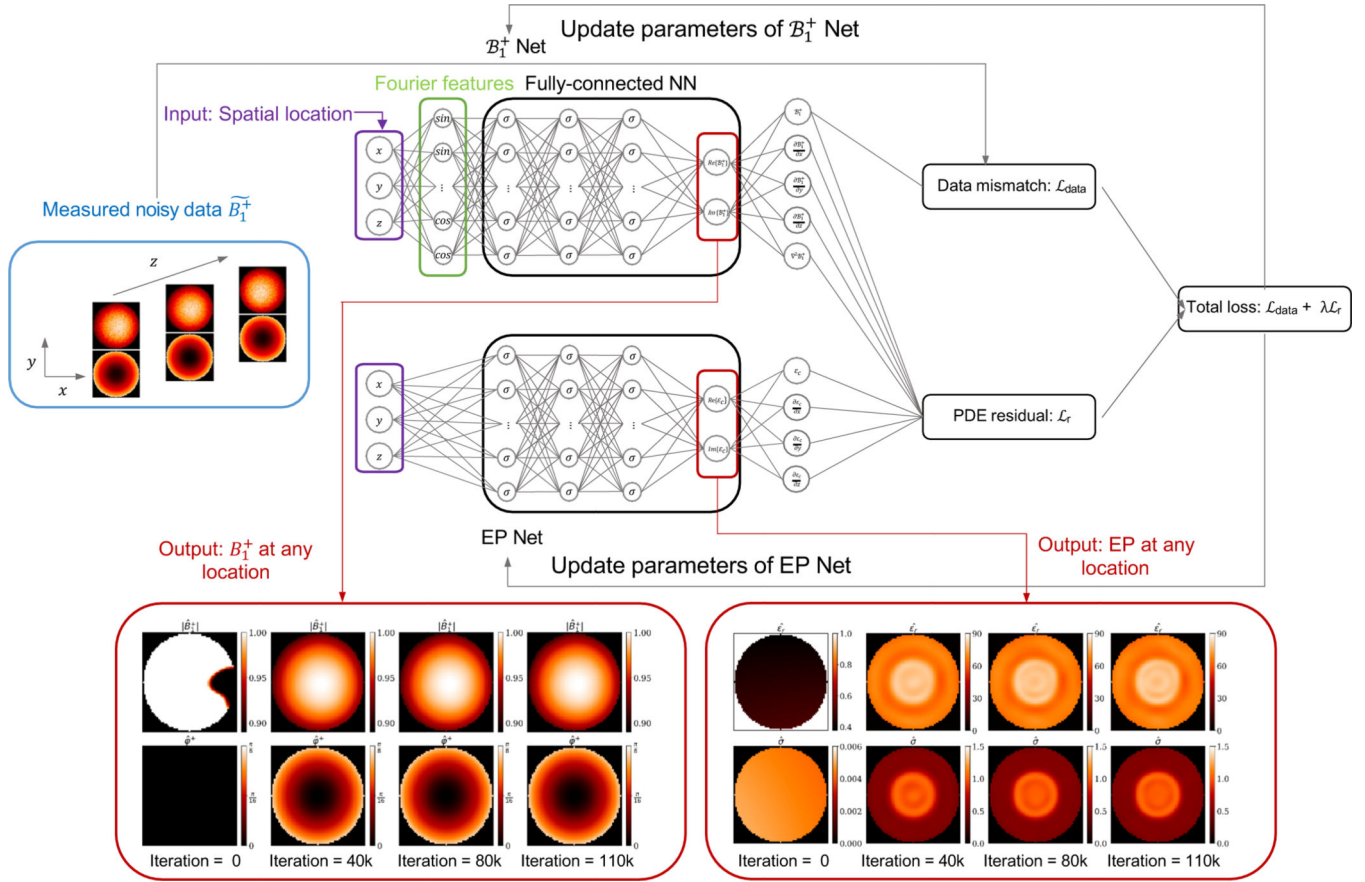
Fig. 1.
PIFON-EPT workflow. Two separate fully-connected neural networks B_1^+ Net ($\mathscr{B}_1^+(\boldsymbol{r}; \boldsymbol{\theta}_1)$) and EP Net ($\mathscr{E}_c(\boldsymbol{r}; \boldsymbol{\theta}_2)$) are defined to take spatial coordinates $\boldsymbol{r} = (x, y, z)$ as inputs and output the corresponding B_1^+ field and the EP distributions, respectively at the same $\boldsymbol{r}$ locations. The B_1^+ Net and EP Net are trained jointly by minimizing a composite loss function that aims to fit the measured $\widetilde{B}_1^+$ data (blue dotted box) while also penalizing the PDE residual. Once trained, the resulting physics-informed B_1^+ Net and EP Net can be used to obtain physically consistent predictions of B_1^+ and EP at any arbitrary 3D location. A representative axial cut of the outputs of the neural networks obtained at different iterations during training is shown at the bottom (red dotted box).
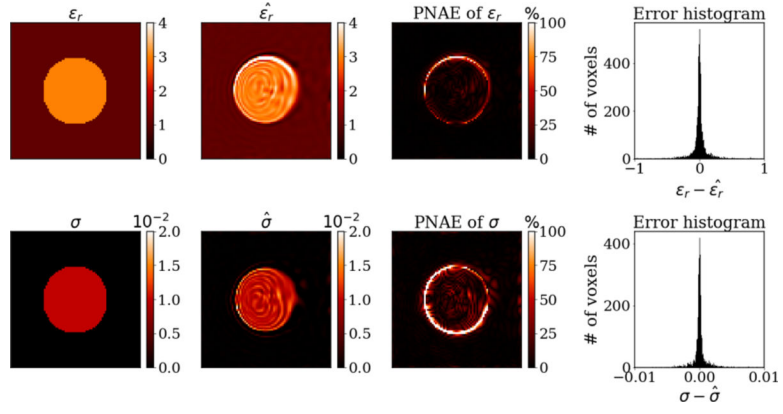
Fig. 2.
EP reconstruction with simplified PIFON-EPT for a representative section of the uniform dielectric cylinder. From left to right, ground truth EP, including relative permittivity (top) and conductivity (bottom), predicted EP using $\widetilde{B}_1^+$ measurements with peak SNR of 200, peak-normalized absolute errors, distribute on of the error in 6561 voxels.
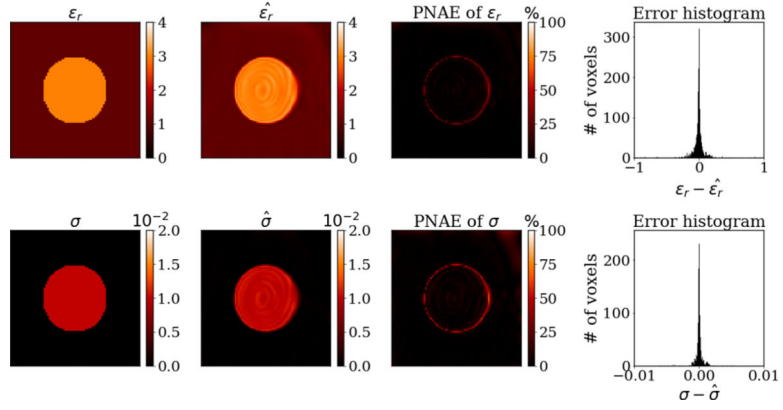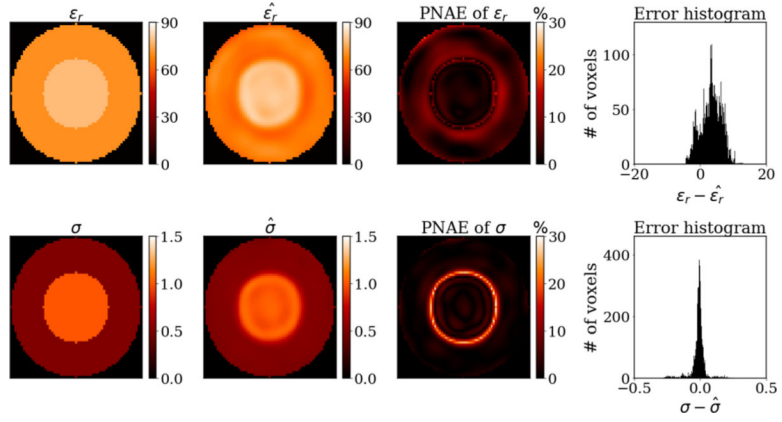
Fig. 3.
EP reconstruction with generalized PIFON-EPT for a representative section of the uniform dielectric cylinder. From left to right, ground truth EP, including relative permittivity (top) and conductivity (bottom), predicted EP using $\widetilde{B}_1^+$ measurements with peak SNR of 200, peak-normalized absolute errors, distribution of the error in 6561 voxels.
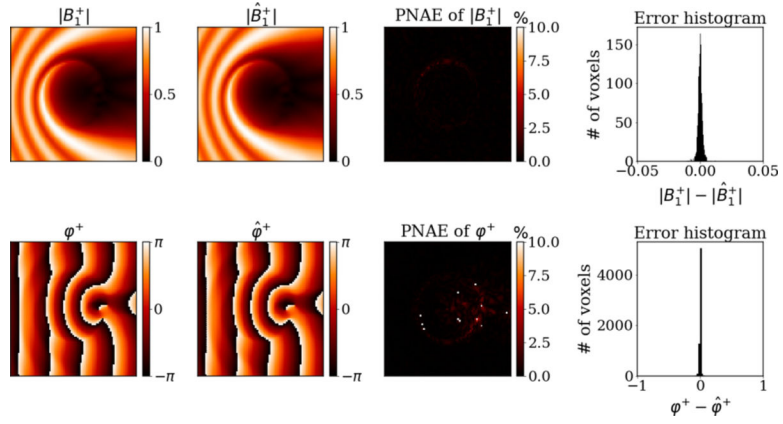
Fig. 4.
Reconstructed B_1^+ with simplified PIFON-EPT for a representative section of the uniform dielectric cylinder. From left to right, ground truth noise-free synthetic B_1^+, including magnitude (top) and transmit phase (bottom), reconstructed B_1^+ from noisy synthetic $\tilde{B}_1^+$ measurements with peak SNR of 200, peak-normalized absolute errors, distribution of the error in 6561 voxels.
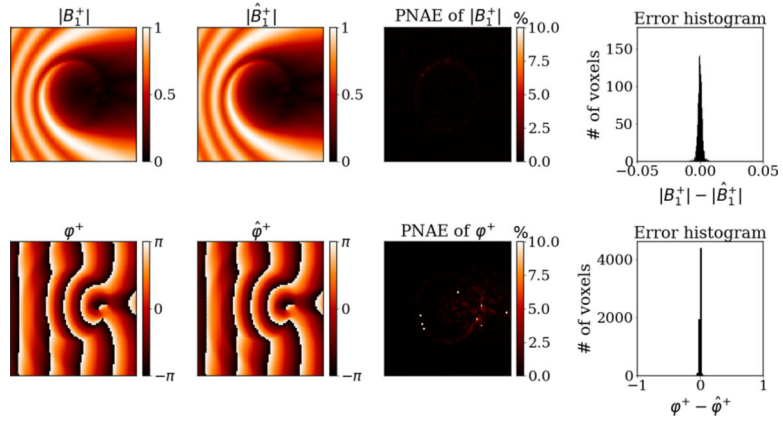
Fig. 5.
Reconstructed B_1^+ with generalized PIFON-EPT for a representative section of the uniform dielectric cylinder. From left to right, ground truth noise-free synthetic B_1^+, including magnitude (top) and transmit phase (bottom), reconstructed B_1^+ from noisy synthetic $\tilde{B}_1^+$ measurements with peak SNR of 200, peak-normalized absolute errors, distribution of the error in 6561 voxels.
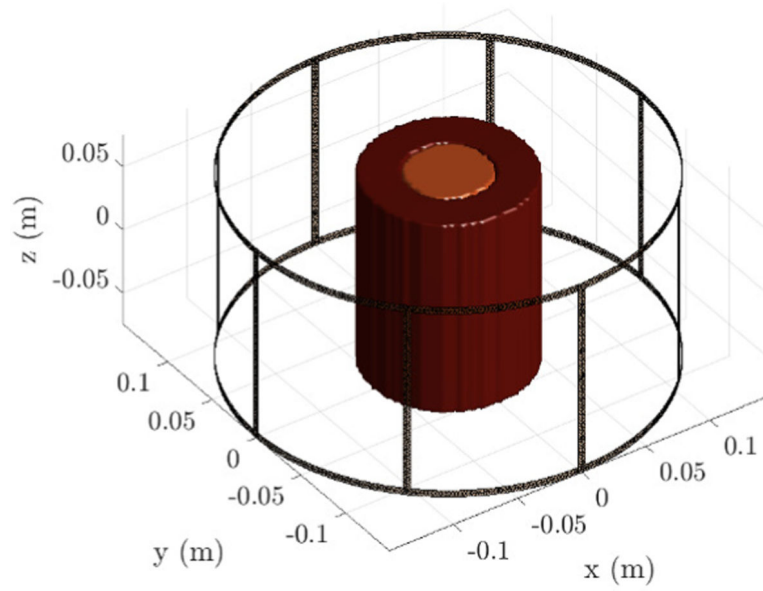
Fig. 6.
Geometry of the high-pass birdcage coil loaded with a two-compartments cylindrical phantom

Fig. 7.
EP reconstructed with generalized PIFON-EPT for the two-compartment cylindrical phantom. From left to right, ground truth EP for the central axial cut of the phantom, including relative permittivity (top) and conductivity (bottom), estimated EP using synthetic $\widetilde{B}_1^+$ measurements with peak SNR of 200, peak-normalized absolute errors, distribution of the error in 31031 voxels.
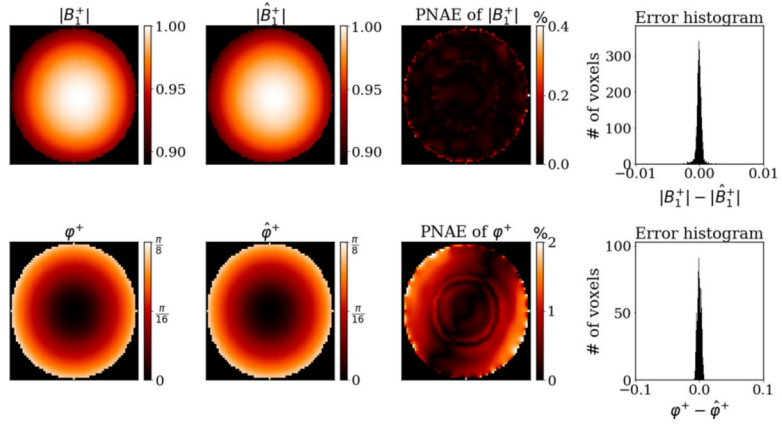
Fig. 8.
Reconstructed B_1^+ with generalized PIFON-EPT for the two-compartment cylindrical phantom. From left to right, noise-free synthetic B_1^+ for the central axial cut, including magnitude (top) and transmit phase (bottom), reconstructed B_1^+ field from noisy $\widetilde{B}_1^+$ measurements, peak-normalized absolute errors, distribution of the error in 31031 voxels.
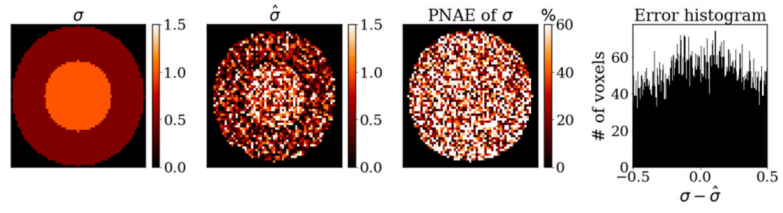
Fig. 9.
Conductivity reconstructed with phase-based H-EPT for the two-compartment cylindrical phantom. From left to right, ground truth conductivity for the central axial cut of the phantom, estimated conductivity using $\widetilde{\varphi}^{\pm}$ measurements with peak SNR of 200, the peak-normalized absolute errors, the distribution of the error in 17423 voxels.
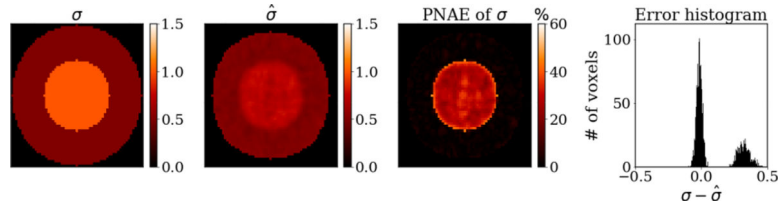
Fig. 10.
Conductivity reconstructed with phase-based CR-EPT for the two-compartment cylindrical phantom. From left to right, ground truth conductivity for the central axial cut of the phantom, estimated conductivity using $\widetilde{\varphi}^{\pm}$ measurements with peak SNR of 200, the peak-normalized absolute errors, the distribution of the error in 11645 voxels.
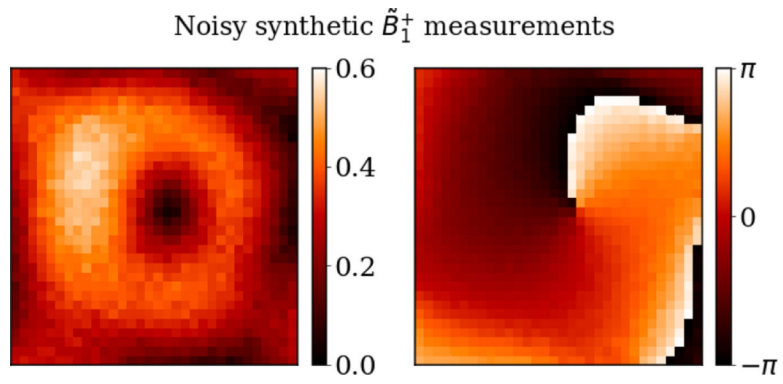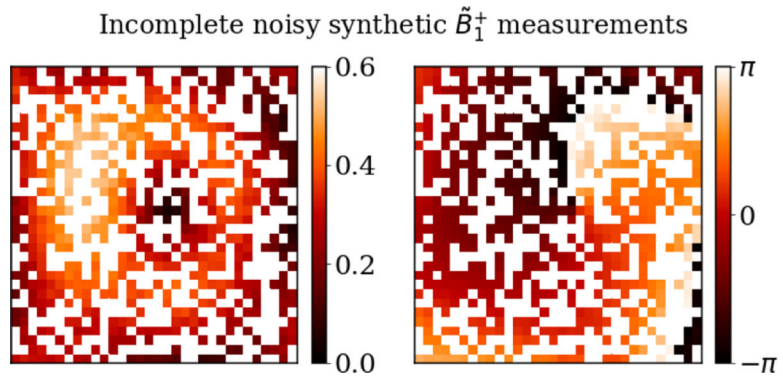
Fig. 11.

Noisy synthetic $\tilde{B}_1^+$ measurements. Magnitude (left) and transmit phase (right) are shown for the central axial cut of the Four-compartment phantom. The peak SNR was set to 50.
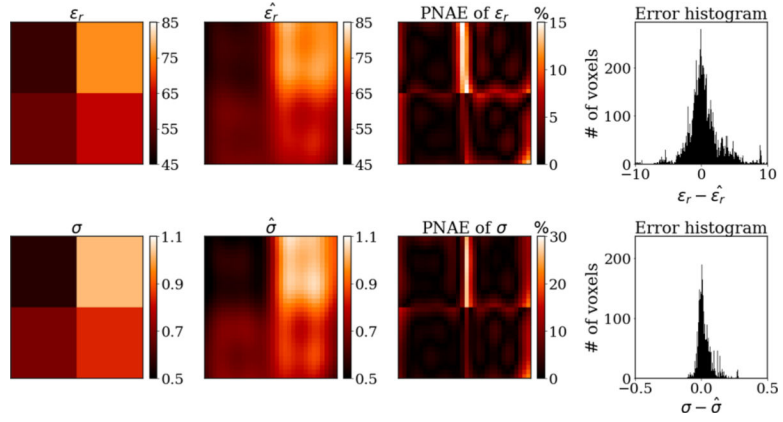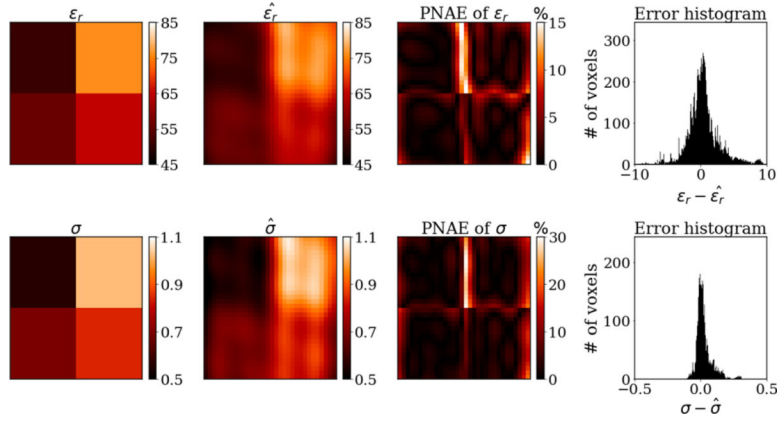
Fig. 12.
EP reconstructed with simplified PIFON-EPT for the four-compartment phantom. From left to right, ground truth EP for the central axial cut of the phantom, including relative permittivity (top) and conductivity (bottom), EP reconstructed from synthetic B_1^+ measurements with peak SNR of 50, peak-normalized absolute errors, error distribution in 32768 voxels.
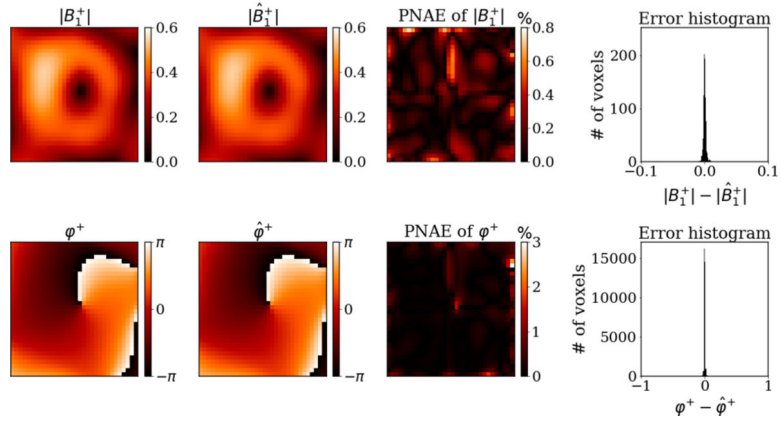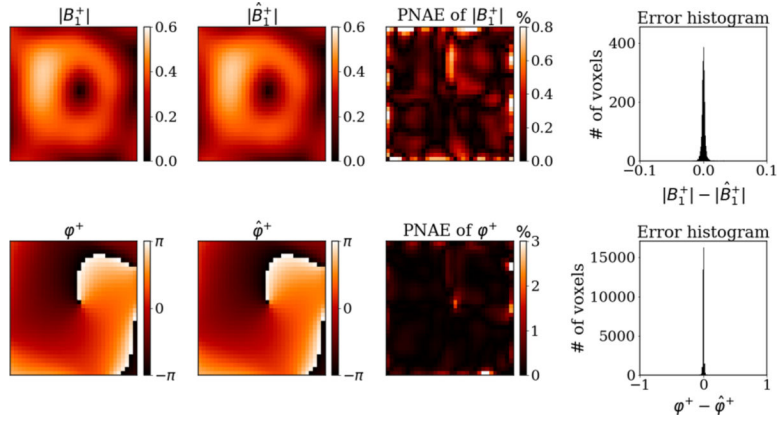
Fig. 13.

Reconstructed B_1^+ with simplified PIFON-EPT for the four-compartment phantom. From left to right, ground truth synthetic B_1^+ for the central axial cut of the phantom, including magnitude (top) and transmit phase (bottom), reconstructed B_1^+ field from noise-corrupted synthetic $\widetilde{B}_1^+$ measurements with peak SNR of 50, the peak-normalized absolute errors, the distribution of the error in 32768 voxels.

Incomplete noisy synthetic $\tilde{B}_1^+$ measurements

Fig. 14.
Incomplete noisy synthetic $\widetilde{B}_1^+$ measurements with 50% of the voxels set to zero. Magnitude (left) and transmit phase (right) are shown for the central axial cut of the Four-compartment phantom. The peak SNR was set to 50.

Fig. 15.
Reconstructed EP with simplified PIFON-EPT for the incomplete four-compartment phantom. From left to right, ground truth EP for the central axial cut of the phantom, including relative permittivity (top) and conductivity (bottom), estimated EP using 50% of $\widetilde{B}_1^+$ with peak SNR of 50, the peak-normalized absolute errors, the distribution of the error in 32768 voxels.

Fig. 16.
Reconstructed B_1^+ with simplified PIFON-EPT for the incomplete four-compartment phantom. From left to right, magnitude (top) and transmit phase (bottom) of the synthetic B_1^+ field for the central axial cut of the phantom, reconstructed B_1^+ field using 50% of $\widetilde{B}_1^+$ with peak SNR of 50, peak-normalized absolute errors, error distribution in 32768 voxels.

TABLE I

Robustness analysis of PIFON-EPT with respect to the noise level

PNAE $\diagdown$ Peak SNR	200	100	50	20
ε_r	2.56%	2.64%	2.47%	2.56%
σ	4.00%	4.10%	4.01%	3.96%
B_1^+	0.15%	0.17%	0.24%	0.49%

TABLE II

<small>PERFORMANCE OF PIFON-EPT WITH RESPECT TO THE PERCENTAGE OF MEASUREMENTS USED AS INPUT FOR THE RECONSTRUCTIONS</small>

PNAE ⟍ % of the Data	80%	50%	20%	10%
ε_r	2.41%	2.49%	2.77%	7.22%
σ	3.94%	4.09%	4.06%	7.58%
B_1^+	0.26%	0.32%	0.57%	2.69%